Chemical Science

ROYAL SOCIETY OF CHEMISTRY

EDGE ARTICLE

View Article Online
View Journal | View Issue

Cite this: *Chem. Sci.*, 2021, **12**, 2189

All publication charges for this article have been paid for by the Royal Society of Chemistry

Hydroxy-bridged resting states of a [NiFe]-hydrogenase unraveled by cryogenic vibrational spectroscopy and DFT computations†

Giorgio Caserta, ‡*[a] Vladimir Pelmenschikov, ‡*[a] Christian Lorent, [a] Armel F. Tadjoung Waffo, [a] Sagie Katz, [a] Lars Lauterbach, [a] Janna Schoknecht, [a] Hongxin Wang, [b] Yoshitaka Yoda, [c] Kenji Tamasaku, [d] Martin Kaupp, [a] Peter Hildebrandt, [a] Oliver Lenz, [a] Stephen P. Cramer *[b] and Ingo Zebger *[a]

The catalytic mechanism of [NiFe]-hydrogenases is a subject of extensive research. Apart from at least four reaction intermediates of H_2/H^+ cycling, there are also a number of resting states, which are formed under oxidizing conditions. Although not directly involved in the catalytic cycle, the knowledge of their molecular structures and reactivity is important, because these states usually accumulate in the course of hydrogenase purification and may also play a role *in vivo* during hydrogenase maturation. Here, we applied low-temperature infrared (cryo-IR) and nuclear resonance vibrational spectroscopy (NRVS) to the isolated catalytic subunit (HoxC) of the heterodimeric regulatory [NiFe]-hydrogenase (RH) from *Ralstonia eutropha*. Cryo-IR spectroscopy revealed that the HoxC protein can be enriched in almost pure resting redox states suitable for NRVS investigation. NRVS analysis of the hydrogenase catalytic center is usually hampered by strong spectral contributions of the FeS clusters of the small, electron-transferring subunit. Therefore, our approach to investigate the FeS cluster-free, ^{57}Fe-labeled HoxC provided an unprecedented insight into the [NiFe] site modes, revealing their contributions in a spectral range otherwise superimposed by FeS cluster-derived bands. Rationalized by density functional theory (DFT) calculations, our data provide structural descriptions of the previously uncharacterized hydroxy- and water-containing resting states. Our work highlights the relevance of cryogenic vibrational spectroscopy and DFT to elucidate the structure of barely defined redox states of the [NiFe]-hydrogenase active site.

Received 10th September 2020
Accepted 11th December 2020

DOI: 10.1039/d0sc05022a

rsc.li/chemical-science

Introduction

Hydrogenases catalyze the reversible cleavage of dihydrogen, thereby making use of earth–abundant transition metals. Among them, O_2-tolerant [NiFe]-hydrogenases are particularly attractive in view of a remarkable catalytic performance under usually inhibiting oxic conditions.[1,2] Buried deeply in the large subunit of the heterodimeric functional unit, the [NiFe] active site contains a Ni and an Fe ion bridged by two cysteine (Cys) residues; two additional terminal Cys bind exclusively to the Ni, while two CN^- and one CO ligands participate in the coordination of the Fe (Fig. 1). H_2 splitting releases two protons that are transferred to nearby proteinaceous H^+ acceptors. The concomitantly released electrons are channeled through an FeS cluster chain located in the small subunit to the hydrogenase's redox partner.[3–5] Although [NiFe]-hydrogenases have been the subject of intensive research for decades, many questions remained open regarding the nature of some resting states as well as catalytically relevant intermediates. Infrared (IR) spectroscopy represents a valuable technique to monitor the redox-sensitive CO and CN^- ligands of the active site, and electron paramagnetic resonance (EPR) spectroscopy provides important electronic and structural information on the active site redox states.[6–8] During catalysis, nickel serves as a redox-active metal center, while iron retains an Fe^{II} low-spin configuration throughout the entire catalytic cycle (Fig. 1, left panel).[1,9] However, some redox states are EPR-silent, and direct IR spectroscopic detection of possible hydride H^- and hydroxy OH^-

[a]*Institut für Chemie, Technische Universität Berlin, Straße des 17. Juni 135, 10623 Berlin, Germany. E-mail: giorgio.caserta@tu-berlin.de; pelmentschikov@tu-berlin.de; ingo.zebger@tu-berlin.de*

[b]*SETI Institute, 189 Bernardo Avenue, Mountain View, CA 94043, USA. E-mail: scramer@seti.org*

[c]*Japan Synchrotron Radiation Research Institute (JASRI), SPring-8, 1-1-1 Kouto, Sayo-gun, Hyogo 679-5198, Japan*

[d]*RIKEN SPring-8 Center, 1-1-1 Kouto, Sayo-cho, Sayo-gun, Hyogo 679-5148, Japan*

† Electronic supplementary information (ESI) available: Materials and methods and supplementary results including Fig. S1–S20 (PDF). Selected DFT normal mode animations (GIF format) relevant to NRVS bands (ZIP archive). Optimized structures (XYZ format) for all DFT-computed models (ZIP archive). See DOI: 10.1039/d0sc05022a

‡ These authors contributed equally.

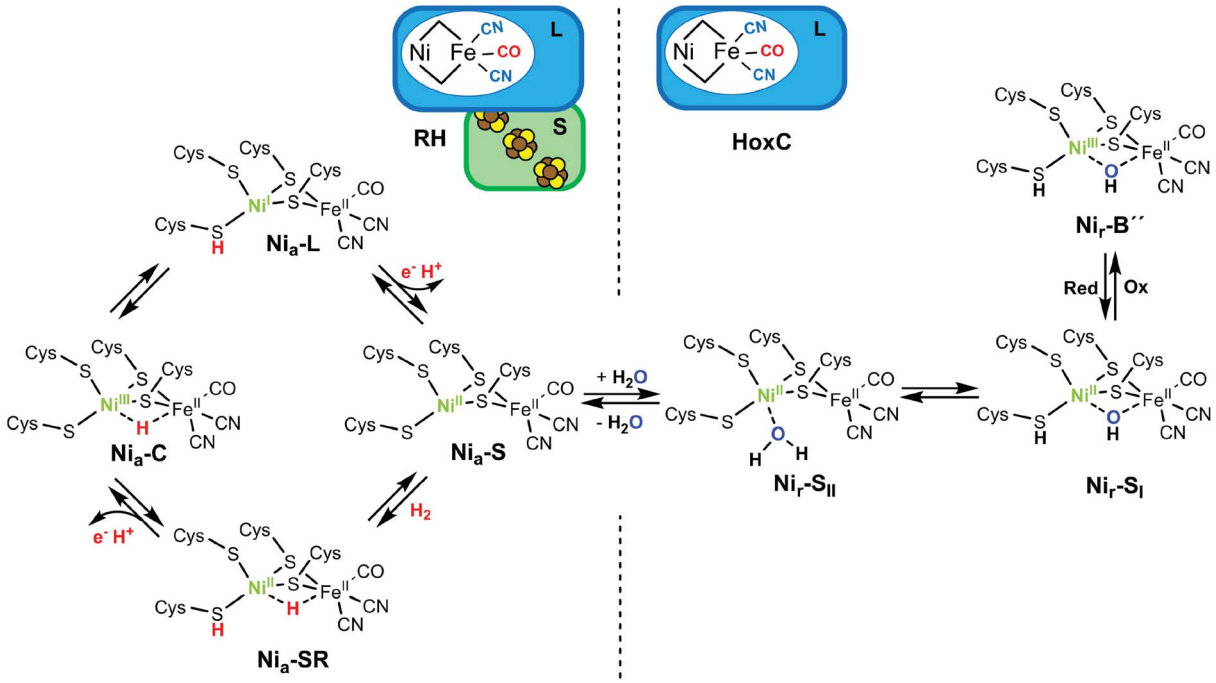

Fig. 1 (Left) Schematic representation of the subunit composition of the RH and the proposed catalytic cycle of [NiFe]-hydrogenases. The states involved in the H_2 transformation include the Ni_a–S intermediate that presumably binds H_2 in the bridging position between the nickel and the iron ions. H_2 splitting results in a two-electron reduced Ni_a–SR state characterized by a bridging hydride. Release of one electron and one proton results in a hydride-carrying Ni_a–C species, which is a tautomeric form of the Ni_a–L state. Release of another electron and a further proton restores the Ni_a–S intermediate.[1,4] Protonation of a terminal cysteine as well as the bridging hydride are highlighted in red. The Ni and its oxidation state are depicted in green. (Right) Schematic representation of the [NiFe]-hydrogenase large subunit HoxC and proposed structures of its resting states. The as-isolated HoxC protein occurs in a mixture of the Ni_r–S_I and Ni_r–S_{II} species. One-electron oxidation results in the formation of the Ni_r–B″ species. Protonation of the terminal cysteine, as found for the Ni_a–SR and the light-induced Ni_a–L intermediates (left panel), and the OH^-/H_2O active site ligands assigned in this work are depicted in bold case letters.

bridging ligands at the active site is hindered by strong spectral contributions of the protein and/or the solvent. Furthermore, resonance Raman (RR) spectroscopy has also been applied for the analysis of metal–ligand vibrations of [NiFe]-hydrogenase intermediate states characterized by a vacant bridging position between Ni and Fe (*i.e.* Ni_a–S and Ni_a–L, Fig. 1).[10,11]

Nuclear resonance vibrational spectroscopy (NRVS) is a synchrotron-based technique that allows selective observation of vibrational modes of Mössbauer-active nuclei. Using the ^{57}Fe nuclear resonance at 14.4 keV, NRVS has provided valuable structural information about [NiFe]-,[12–14] [FeFe]-,[15,16] and [Fe]-hydrogenases.[17] A typical NRV spectrum of [NiFe]-hydrogenase comprises dominant bands of Fe–S(–Fe) stretching and bending modes in the region between 100 and 420 cm^{-1}, which are mostly related to the FeS clusters of the electron transport chain, as well as Fe–CO/CN stretching and bending modes of the [NiFe] active site in the 400–650 cm^{-1} spectral region. Most of the iron atoms in the enzyme are located in the FeS clusters; therefore their spectral contributions surpass the signals of the single active site iron. This results often in poorly resolved signals of the Fe–CO/CN modes, which have a relatively low intensity. Furthermore, certain bands related to the FeS clusters and the [NiFe] active site are superimposed, hindering their unambiguous assignment.[12,14,18] Nevertheless, a combined approach of NRVS and density functional theory (DFT) has provided significant structural details of the [NiFe] active site in catalytic intermediates, revealing the existence of a hydride-containing Ni_a–SR intermediate.[13]

Apart from H_2-cycling intermediates, several resting states are formed under non-turnover conditions.[1] Although these states are not directly involved in the catalysis, the knowledge of their molecular structure is important, because they accumulate in the course of hydrogenase purification and often require extensive reactivation procedures. Additionally, they may also play a role *in vivo* during hydrogenase maturation protecting the active site from redox inactivation.[19]

Recently, we isolated the catalytic subunit HoxC from the O_2-tolerant regulatory [NiFe]-hydrogenase (RH) of *Ralstonia eutropha*. HoxC hosts exclusively the [NiFe] active site and exhibits little activity due to the predominance of inhibited resting states.[19] Therefore, the HoxC protein is an ideal target for a selective and detailed spectroscopic investigation of the catalytic center in its resting states (Fig. 1) without interference from the auxiliary FeS clusters. In this work, we applied low-temperature IR and NRVS techniques together with DFT calculations on the ^{57}Fe-labeled HoxC protein to gain structural information of these so-far poorly characterized [NiFe]-hydrogenase states. We uncovered the vibrational bands of the active site in a broad spectral range, previously superimposed by the Fe–S vibrations. This enabled us to define new

structural determinants of the catalytic center, namely a bridging hydroxy-ligand and a protonated Ni-bound cysteine residue, as key elements of the two resting states. These new finding may represent benchmarks for future NRVS studies on site-selectively labeled hydrogenases as well as biomimetic [NiFe] compounds.

Results and discussion

IR detection of CO and CN^- ligands of the [NiFe] active site at ambient and cryogenic temperatures

The as-isolated HoxC protein ($HoxC_{ai}$) contains a stoichiometric amount of the [NiFe] active site, which resided in the diamagnetic and isoelectronic Ni_r–S_I and Ni_r–S_{II} states at ambient temperature (Fig. 1 and 2a).[1,19] A previous study showed that these states can be partially interconverted by shifting the pH of the buffer.[19] This has been interpreted with the presence of a protonatable bridging ligand at the active site, attributed to a hydroxy (OH^-) group (Fig. 1).[20–22] Native RH, for comparison, resided preferentially in the Ni_a–S state characterized by a vacant bridging position and a CO absorption in the IR spectrum at 1943 cm^{-1}, which remains stable over a broad pH range (Fig. S1†).[19,23] As NRVS is conducted under cryogenic conditions (estimated sample temperature of 40–80 K), it is advisable to record the corresponding IR spectra of the HoxC and RH proteins at similarly low temperatures to allow a direct comparison of the two spectroscopic techniques. In fact, the mixture of the Ni_r–S_I and Ni_r–S_{II} states, observed for $HoxC_{ai}$ at 283 K, converted into an almost pure Ni_r–S_I species at 85 K characterized by a CO absorption at 1955 cm^{-1} (Fig. 2b). According to our previous interpretation,[19] the Ni_r–S_I and Ni_r–S_{II} species just differ in the protonation state of the bridging ligand (OH^- *vs.* H_2O). Thus, cryogenic temperatures seem to stabilize the hydroxy ligand (Fig. 1), which is presumably related to the temperature-dependent changes of the active site surrounding. The enrichment of the Ni_r–S_I state turns out to be reversible. Indeed, setting the temperature of the HoxC sample to 298 K (RT) restored the original Ni_r–S_I/Ni_r–S_{II} ratio (Fig. S2†). Native RH, by contrast, retained a single CO absorption at 1946 cm^{-1} in the IR spectrum, *i.e.* it maintained the Ni_a–S state at 85 K (Fig. 2b). Thus, HoxC and RH exhibit different IR spectra both at room temperature and under cryogenic conditions, reflecting at least slightly divergent active site structures.

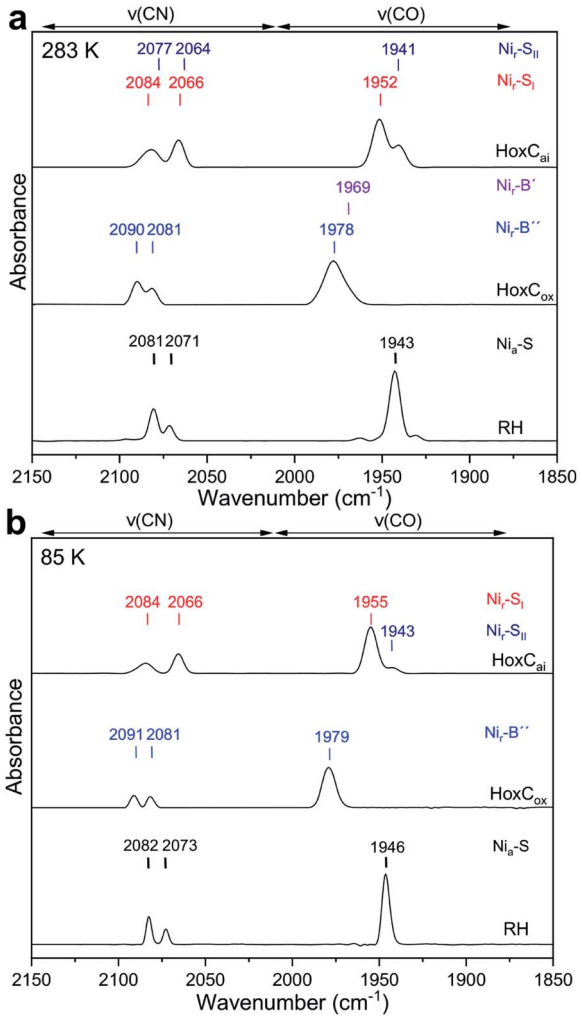

Fig. 2 IR spectra of $HoxC_{ai}$, $HoxC_{ox}$ and RH (top to bottom) taken at 283 K and 85 K. (a) IR spectral region characteristic of CO and CN stretching modes recorded at 283 K. The spectrum of $HoxC_{ai}$ exhibits spectral contributions of the Ni_r–S_I (red) and Ni_r–S_{II} (dark blue) resting states, respectively. The spectrum of RH is dominated by signals attributed to the Ni_a–S state (labeled in black). The IR data of $HoxC_{ox}$ comprise contributions from two paramagnetic oxidized Ni_r–B′ (minor species) and Ni_r–B″ states labeled in purple and blue, respectively. (b) IR spectral region characteristic of CO and CN stretching modes recorded at 85 K for the same samples. Contributions from the corresponding CN absorptions of $Fe(CN)_6^{3-}$ and $Fe(CN)_6^{2-}$ present in the chemically oxidized $HoxC_{ox}$ were subtracted for the sake of clarity.[19]

In our previous work, we showed that $HoxC_{ai}$ can be oxidized by ferricyanide, revealing a species denoted as $HoxC_{ox}$.[19] According to X-ray, EPR and DFT studies, standard [NiFe]-hydrogenases form paramagnetic Ni^{III} species such as the Ni_r–B state upon oxidation (Fig. 1).[1,24–26] The IR spectrum of $HoxC_{ox}$, recorded at room temperature, displayed bands assigned to Ni_r–B-like species termed Ni_r–B′ and Ni_r–B″, respectively.[19] Low-temperature IR measurements performed on $HoxC_{ox}$ revealed the Ni_r–B″ state, characterized by a CO absorption at 1979 cm^{-1}, as the predominant species at 85 K (Fig. 2b). The oxidation of the nickel site was confirmed by EPR measurements (Fig. S3†).[19] The fact that almost pure Ni_r–S_I and Ni_r–B″ states were observed in $HoxC_{ai}$ and $HoxC_{ox}$, respectively, allowed for establishing DFT models, which were subsequently used to interpret the low-temperature IR and NRV spectra.

DFT modeling of the HoxC active site in the Ni_r–S- and Ni_r–B-like states

DFT calculations were used to model the structural details and vibrational spectra of the [NiFe] active site in the $HoxC_{ai}$/$HoxC_{ox}$ proteins. In the absence of experimentally resolved crystallographic structures of either HoxC or native RH, the DFT modeling was based on the corresponding X-ray structure of the membrane-bound hydrogenase (MBH) from the same organism.[27] The model setup is described in detail in the ESI† Materials and methods. In comparison to the large subunit of

MBH, our HoxC homology model revealed a larger active site pocket with a lower number of contacts between the protein side chains and the metal ligands (Fig. S4†). The DFT calculations were performed for the reduced, diamagnetic Ni_r–S-like [$Ni^{II}Fe^{II}$] species with an overall spin of zero and for the oxidized, paramagnetic Ni_r–B-like [$Ni^{III}Fe^{II}$] state with a spin of 1/2. According to previous structural predictions for the reversibly inhibited ready-states of [NiFe]-hydrogenases,[1,28,29] our models contained a bridging hydroxy (μOH subscript in the model notations) ligand at the active site (Fig. S5–S7†). For the Ni_r–S species, local energy minima were also obtained with a water molecule serving as either a metal-bridging (μH_2O), a Ni-terminal (Ni–H_2O),[28,29] or an Fe-terminal (Fe–H_2O) ligand (Fig. S8–S10†). All models revealed a hydrogen bonding between the guanidinium group of the conserved arginine residue and the alternative metal-bound μOH/H_2O species (Fig. S6–S10†). The DFT model set was further extended by considering the Ni-bound terminal cysteine Cys479 with either a protonated thiol (SH superscript in the model notations), as, *e.g.*, in the Ni_r–$S^{SH}_{\mu OH}$ model shown in Fig. 3a, or a deprotonated thiolate (S^-, as shown in Fig. 3b and S6–S10†). This is in line with the proposed protonation of the corresponding cysteine residue in the catalytically relevant Ni_a–SR and Ni_a–L states of [NiFe]-hydrogenases.[30–34] We also examined the second Ni-bound terminal cysteine Cys60 as a possible protonation site. The corresponding Ni_r–$S^{Cys60\text{-}SH}_{\mu OH}$ model is shown in Fig. S6.†

Notably, the structural optimization of the Ni_r–$S_{\mu OH}$ models revealed an over-elongated bond between the Ni^{II} ion and the bridging sulfur ligand of Cys482,[19,28,35] whose length depended on the protonation state of the Ni-terminal cysteines. The Ni_r–$S^{SH}_{\mu OH}$, Ni_r–$S^{Cys60\text{-}SH}_{\mu OH}$ and Ni_r–$S^{S-}_{\mu OH}$ models yielded $Ni^{II}\cdots$S(Cys482) distances of 2.7, 2.8 and 3.0 Å, respectively, consistent with an essentially lost coordination. All other Ni/Fe–S (Cys ≠ Cys482) distances remained within a narrow bonding range of ~2.2–2.4 Å across the entire model set. No bond elongation or lost coordination between the Ni^{III} ion and the bridging sulfur ligand of Cys482 was found for the Ni_r–$B_{\mu OH}$ models, as, *e.g.*, in the Ni_r–$B^{SH}_{\mu OH}$ model (Fig. 3c), in line with available crystallographic data.[24] To account for the flexibility of the Ni coordination sphere, the present DFT models included explicitly the two short CXXC protein sequence spacers spanning the two cysteine pairs ligating the nickel (Fig. S4†).

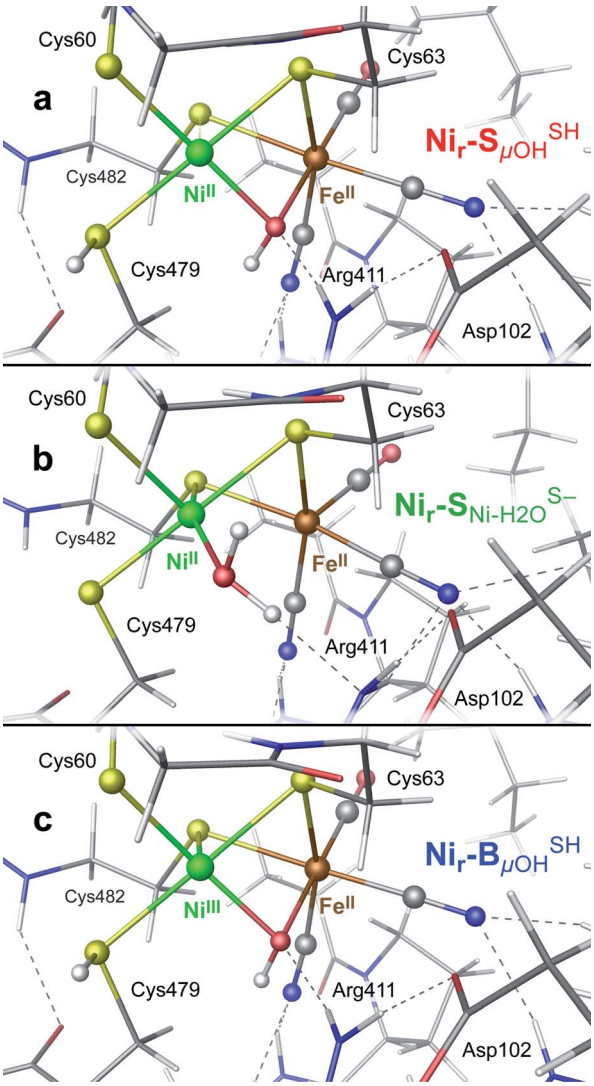

Fig. 3 DFT models: (a) Ni_r–$S^{SH}_{\mu OH}$ of the reduced Ni_r–S_I state, (b) Ni_r–$S^{S-}_{Ni-H_2O}$ of the reduced Ni_r–S_{II} state, and (c) Ni_r–$B^{SH}_{\mu OH}$ of the oxidized Ni_r–B″ state, displaying the [NiFe] cofactor metal ligands and their contacts with the nearby side chains in HoxC. For alternative models and the entire HoxC homology model employed, see Fig. S4–S10.†

DFT reproduces the experimental IR spectra of the Ni_r–S_I and Ni_r–B″ states of HoxC

DFT calculations based on the Ni_r–$S^{SH}_{\mu OH}$ and Ni_r–$B^{SH}_{\mu OH}$ models (Fig. 3a and c, or S6 and S7†) predict CO and CN stretching frequencies as well as relative IR intensities close to those detected in the low-temperature IR measurements (Fig. 2b, S11a and b†). While the absolute positions of the DFT-simulated CO and CN bands in proteins commonly rely on a linear fit procedure (described in the ESI† Materials and methods), the corresponding direction of band shifts is independent of the fitting procedure and reflects a polarization of the Fe-bound CO/CN^- ligands. Thus, a charge increase of 1+ per active site unit results in a predicted blue-shift of the CO stretching frequency of ~20–30 cm^{-1}. This is reflected by the simulated IR bands from a series of models at three levels of charge, *i.e.* (i) Ni_r–$S^{S-}_{\mu OH}$, (ii) Ni_r–$B^{S-}_{\mu OH}$/Ni_r–$S^{SH}_{\mu OH}$ and (iii) Ni_r–$B^{SH}_{\mu OH}$ (Fig. S11†). The blue shift of ~20–30 cm^{-1} is in a good agreement with the experimentally monitored spectral shift of 24 cm^{-1} observed for the Ni_r–S_I ($HoxC_{ai}$) and Ni_r–B″ ($HoxC_{ox}$) states (Fig. S11a and b†). This is consistent with the oxidation of the nickel ion from Ni^{II} to Ni^{III} for the Ni_r–S_I to Ni_r–B″ conversion (Fig. S3†),[22,36,37] assuming that the protonation status of Cys479 was unchanged. Altogether, the experimental and theoretical data are consistent with a total charge increase of 1+ at the [NiFe] active site when moving from $HoxC_{ai}$ to $HoxC_{ox}$. Thus, the comparison of the experimental and DFT-computed IR spectra does not allow a conclusive statement whether or not Cys479 is protonated.

The low-temperature IR spectrum of $HoxC_{ai}$ also revealed traces of the Ni_r–S_{II} species, identified through the CO band at 1943 cm^{-1}, which is shifted just by 12 cm^{-1} compared to the CO band at 1955 cm^{-1} of Ni_r–S_I (Fig. 2b). Therefore, the Ni_r–S_I and Ni_r–S_{II} states carry rather an identical charge. Among the different Ni_r–S models explored, a red-shifted CO band with the same active site charge was computed assuming a terminal H_2O ligand at the Ni ion and a deprotonated Cys479 (Ni_r–$S^{S-}_{Ni-H_2O}$, Fig. 3b, S12† and 1). The relative energy difference between the Ni_r–$S^{S-}_{Ni-H_2O}$ and Ni_r–$S^{SH}_{\mu OH}$ models is just 2.0 kcal mol^{-1}. Thus, the corresponding Ni_r–S_{II} and Ni_r–S_I species may coexist in a temperature-dependent dynamic equilibrium with a slight preference for Ni_r–S_I (Fig. S2†). Yet, an alternative rationalization of the minor red-shifted Ni_r–S_{II} is that it represents a species singly deprotonated with regard to the Ni_r–S_I state, still carrying the bridging hydroxy ligand (Ni_r–$S^{S-}_{\mu OH}$ *vs.* Ni_r–$S^{SH}_{\mu OH}$, Fig. S11a†). A recent computational study supported the Ni_r–$S^{SH}_{\mu OH}$ and Ni_r–$S^{S-}_{Ni-H_2O}$ active site assignment for the Ni_r–$S_{I/II}$ states.[35]

Experimental and DFT-computed NRV spectra of the active site in $HoxC_{ai}$ and $HoxC_{ox}$ proteins

The NRV spectra of ^{57}Fe-enriched $HoxC_{ai}$ and RH are shown in Fig. 4. As native RH has three [4Fe4S] clusters, bands originating from the FeS clusters dominate the corresponding spectrum. The spectral contributions of the [NiFe] site are relatively weak and visible only in the high-frequency region of 420–600 cm^{-1} (Fig. 4).[12] Further details about the NRVS characterization of RH are provided in the ESI Supplementary results and Fig. S13 and S14.† The most intense active site bands in RH are detected at 553 cm^{-1} and 596 cm^{-1} and are attributed mainly to Fe–CO stretching and bending modes.[12] Bands below 530 cm^{-1}, which are due to Fe–CN and mixed Fe–CO/CN modes, could not be properly resolved due to their relatively low intensity.

NRV spectra for the $HoxC_{ai}$ and $HoxC_{ox}$ samples were obtained under conditions identical to those applied for the cryogenic IR measurements. The NRV spectrum of the $HoxC_{ai}$ sample, which mostly resided in the Ni_r–S_I state (Fig. 2b), comprises main bands at 554, 600 and 612 cm^{-1} in addition to features at 507, 474, 445 and 427 cm^{-1} (Fig. 4). The corresponding spectrum of $HoxC_{ox}$, which mostly resided in the Ni_r–B″ state (Fig. 2b), is shown in Fig. S15.† Due to the absence of the FeS clusters, the observed bands could be attributed exclusively to the [NiFe] center. This also led to a notable increase of the intensity of the characteristic Fe–CO/CN vibrations in the ~400–600 cm^{-1} region compared to the RH spectrum (Fig. 4, red shaded rectangle). Moreover, we also observed the spectral contributions of the active site in the low-frequency region with a main band at 180 cm^{-1}. This spectral region of the HoxC NRV spectrum (Fig. 4, 5 and S15†) is shaped by the (i) torsional/'breathing' modes of the cofactor (~150–220 cm^{-1}), (ii) [NiFe] core displacements relative to the protein framework (~50–150 cm^{-1}), and (iii) displacements of the cofactor in phase with the nearby side chains or 'acoustic' modes (below ~50 cm^{-1}). The intermediate-frequency region (~250 to 400 cm^{-1}), containing high-intensity FeS cluster bands in the

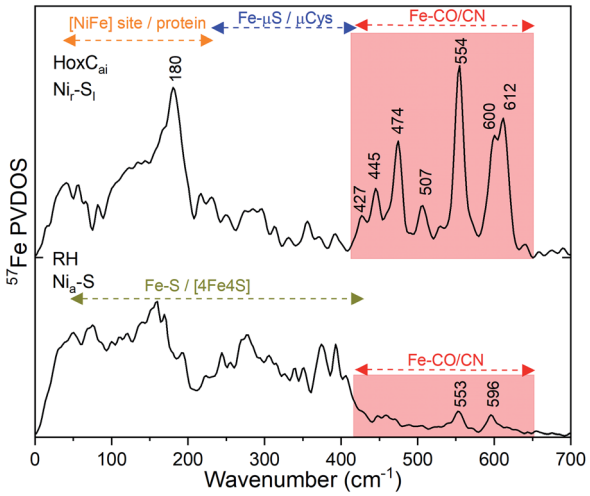

Fig. 4 NRVS partial vibrational density of states (PVDOS) of ^{57}Fe-labeled RH (bottom) and its large subunit HoxC (top), in their isolated forms, normalized to an integrated PVDOS of 3. Different spectral regions are indicated with arrows using the following color code: red, bands related to Fe–CO/CN of the [NiFe] active site; orange, bands related to [NiFe] site/protein modes; blue, bands related to Fe–μS modes involving bridging cysteines; olive, bands related to the Fe–S modes of the [4Fe4S]-clusters. Representative bands in the RH and HoxC spectra are labeled with numbers in black. The corresponding NRVS data including the error bars are presented in Fig. S20.†

uniformly ^{57}Fe-labeled RH spectrum, is largely free of distinct bands of HoxC. The only vibrations of a similar type in the active site are Fe–μS(Cys) stretching modes of the two bridging cysteines, detectable in the region of 270–380 cm^{-1} (Fig. S19g†). These contributions cannot be detected in the presence of (NRV-active) FeS clusters (Fig. 4). Consistent with low-temperature IR spectroscopic measurements (Fig. 2b), the spectral differences of the NRVS data indicate that the catalytic centers of RH (Ni_a–S) and $HoxC_{ai}$ (Ni_r–S_I) reside in different states (Fig. 1).

The DFT models described above (Fig. S6–S10†) were used to generate the ^{57}Fe-PVDOS profiles of the $HoxC_{ai}$ and $HoxC_{ox}$ proteins in the Ni_r–S_I and Ni_r–B″ states, respectively (Fig. S16 and S17†). Fig. 5 shows a comparison of the $HoxC_{ai}$ experimental spectrum (0–700 cm^{-1} region) with the DFT-calculated spectra based on the Ni_r–S models. The computed data based on the Ni_r–$S^{S-}_{\mu OH}$ and Ni_r–$S^{SH}_{\mu OH}$ models – both carrying a bridging hydroxy group – reproduce the experimental spectrum very well (Fig. 5a, S16 and S18†).

Yet, an alternative hydroxy-bridged Ni_r–S model in which Cys60 is protonated (Ni_r–$S^{Cys60\text{-}SH}_{\mu OH}$) revealed a distinct ~20 cm^{-1} splitting of the high-intensity ~550 cm^{-1} band and is therefore rather incompatible with the experimental spectrum (Fig. 5b). All the other models, carrying either bridging H_2O (Ni_r–$S^{S-}_{\mu H_2O}$ and Ni_r–$S^{SH}_{\mu H_2O}$, Fig. 5c), a terminal, Fe-bound water molecule (Ni_r–$S^{S-}_{Fe-H_2O}$ and Ni_r–$S^{SH}_{Fe-H_2O}$, Fig. 5d) or a terminal, Ni-bound water molecule (Ni_r–$S^{S-}_{Ni-H_2O}$ and Ni_r–$S^{SH}_{Ni-H_2O}$, Fig. 5e), led to ^{57}Fe-PVDOS signatures with an inferior match to the experimental spectrum of $HoxC_{ai}$. A closer examination of the low-frequency region (0–200 cm^{-1}) revealed that the Ni_r–

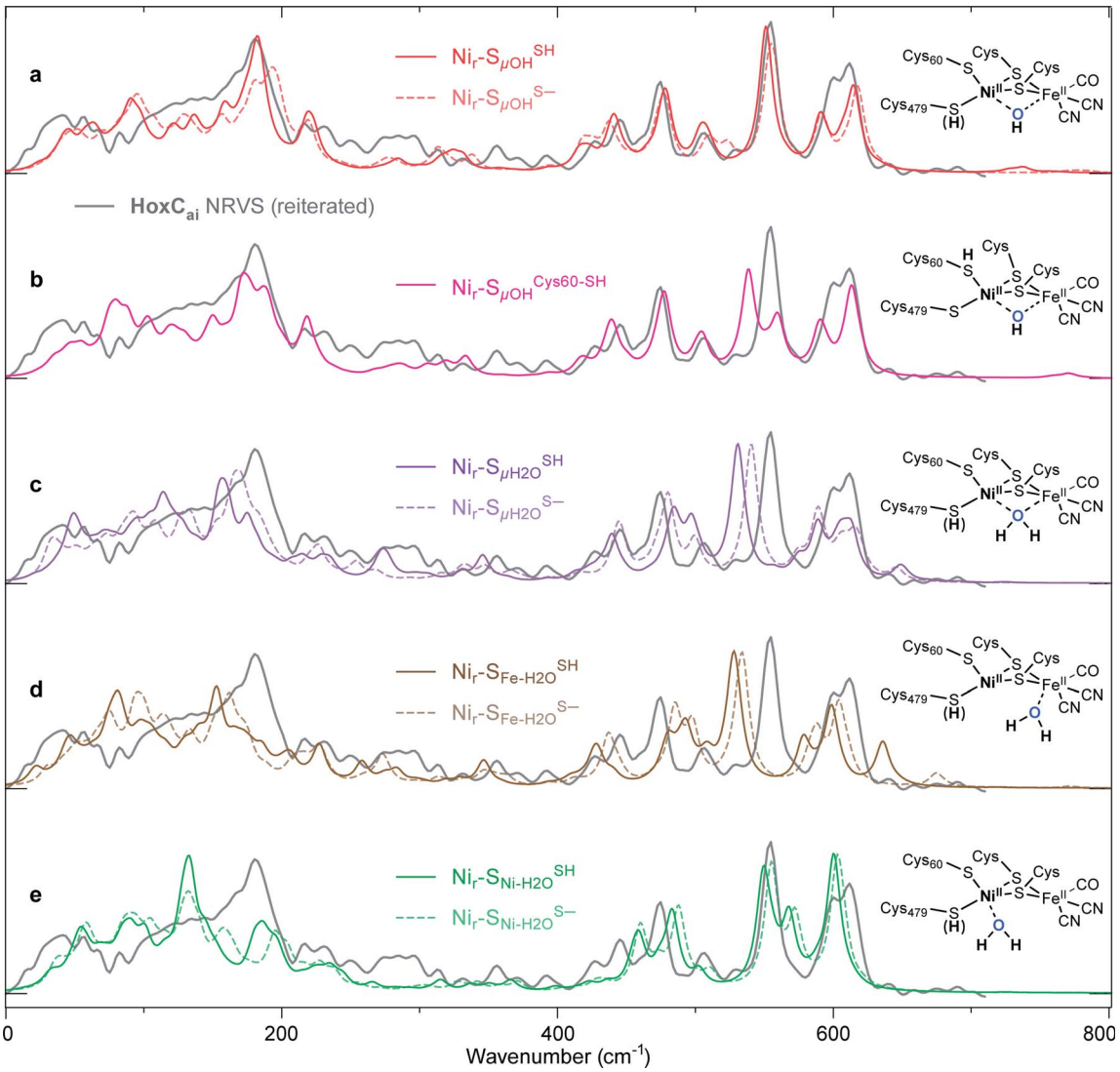

Fig. 5 Comparison of the experimental NRV spectrum of the $HoxC_{ai}$ sample (Ni_r–S_I, grey trace reiterated in (a–e)) overlaid with the corresponding DFT-calculated ^{57}Fe-PVDOS bands using alternative [$Ni^{II}Fe^{II}$] models, schematically shown on the right side of the spectra. The DFT spectra derived using either protonated (solid lines) or deprotonated (broken lines) Cys479 are shown for the following models: (a) best-fit Ni_r–$S^{SH}_{\mu OH}$ and Ni_r–$S^{S-}_{\mu OH}$ (Fig. S6†); (c) Ni_r–$S^{SH}_{\mu H_2O}$ and Ni_r–$S^{S-}_{\mu H_2O}$ (Fig. S8†); (d) Ni_r–$S^{SH}_{Fe-H_2O}$ and Ni_r–$S^{S-}_{Fe-H_2O}$ (Fig. S9†); (e) Ni_r–$S^{SH}_{Ni-H_2O}$ and Ni_r–$S^{S-}_{Ni-H_2O}$ (Fig. S10†). The DFT spectrum derived from the alternative hydroxy model with protonated Cys60, Ni_r–$S^{Cys60-SH}_{\mu OH}$, is highlighted in (b). Both μOH^- models in (a) reproduce the experimental data in the Fe–CO/CN region above 400 cm^{-1}. Minor differences in the low-frequency spectral region around 180 cm^{-1} (Fig. S16†) strengthen the Ni_r–$S^{SH}_{\mu OH}$ model, in line with the better prediction of the experimental IR absorptions for the CO and CN stretching modes (Fig. S11a†).

$S^{SH}_{\mu OH}$ model, which carries a protonated Cys479, provides a more accurate fit (solid line in Fig. 5a) to the experimental spectrum than the unprotonated form (Ni_r–$S^{S-}_{\mu OH}$, dotted line in Fig. 5a, see also Fig. S16†). In this respect, the shape and position of the high-intensity band at ~180 cm^{-1} in the calculated HoxC spectrum were found remarkably sensitive to the specific μOH^-/(μ/Ni-/Fe-)H_2O ligand coordination as well as to the protonation of the Ni-bound terminal cysteine(s) (Fig. 5 and S16†).

Analogously to low-energy NRVS maxima in the spectral region characteristic of FeS clusters, preferentially attributed to S–Fe–S bending vibrations (Fig. S13 and S14a†),[14,38] the active site normal modes forming the ~180 cm^{-1} band comprise 'delocalized' Cys(S)–Ni/Fe–(S)Cys bending modes involving entire side chain motions of the four cysteines. Additional details on the effects influencing the ^{57}Fe-PVDOS profiles are provided in the ESI† Supplementary results. The experimental spectrum of $HoxC_{ox}$ was best reproduced by DFT-computed data based on the Ni_r–$B^{SH}_{\mu OH}$ model, which contains a protonated Cys479 cysteine (Fig. S17†). Thus, the Ni_r–S_I and Ni_r–B″ states differ only in the oxidation level of the Ni ion, and the Ni_r–S_I to Ni_r–B″ transition represents a one-electron oxidation of Ni^{II} to Ni^{III}.[20,22,36] This is fully consistent with our DFT-supported IR analysis (Fig. 2b and S11†) and the EPR measurements (Fig. S3†). Accordingly, the NRVS data of the $HoxC_{ox}$ sample revealed red-shifts of 8–15 cm^{-1} of bands in the region above

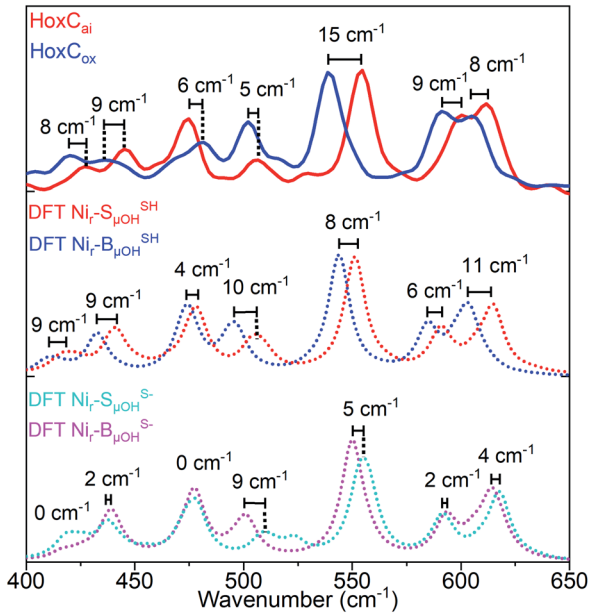

Fig. 6 Comparison of the experimentally observed and DFT-calculated ^{57}Fe-PVDOS bands in the 400–650 cm^{-1} spectral region for HoxC$_{ai}$ and HoxC$_{ox}$. Experimental spectra (top: red trace, HoxC$_{ai}$; blue trace, HoxC$_{ox}$) are compared to their DFT-calculated counterparts based on the corresponding models that contain either protonated (middle: Ni$_r$–S$_{\mu OH}^{SH}$ and Ni$_r$–B$_{\mu OH}^{SH}$ states) or deprotonated Ni-bound terminal cysteine (bottom: Ni$_r$–S$_{\mu OH}^{S-}$ and Ni$_r$–B$_{\mu OH}^{S-}$ states). Bands calculated using Ni$_r$–S$_{\mu OH}^{SH}$ and Ni$_r$–B$_{\mu OH}^{SH}$ models are in better agreement with the NRVS data, including their shift magnitudes marked in the figure. The corresponding NRVS data including the error bars are presented in Fig. S20.†

500 cm^{-1} dominated by the Fe–CO stretching vibrations compared to the HoxC$_{ai}$ sample (Fig. 6), thereby reflecting the oxidation of the active site.

The red-shifts of this magnitude are predicted by the corresponding DFT models with protonated Cys479 (Ni$_r$–S$_{\mu OH}^{SH}$ → Ni$_r$–B$_{\mu OH}^{SH}$). The related models without terminal cysteine protonation (Ni$_r$–S$_{\mu OH}^{S-}$ → Ni$_r$–B$_{\mu OH}^{S-}$) revealed smaller band shifts, which do not reflect the experimental data (Fig. 6). Notably, while the oxidation of the active site led to a red-shift of the Fe–CO/CN vibrations in NRVS (Fig. 6), a blue-shift was observed for the IR stretching frequencies of the active site CO/CN$^-$ ligands (Fig. 2b). This can be rationalized by charge polarization effects at the Fe site. Stronger bonds within the diatomic ligands, reflected by the blue-shifted IR bands related to the CO and CN stretching vibrations, imply, in turn, weaker Fe–CO/CN bonds, resulting in a red-shift of the corresponding NRVS bands. The accurate prediction of this redox-dependent vibrational shift relies on the inclusion of explicit interactions between the HoxC protein environment and the [NiFe]-cofactor, as confirmed by our computational test using an alternative minimal model omitting all the residues except the four cysteines directly coordinating the two metals (ESI Supplementary results and Fig. S18c†).

Taking advantage of the good agreement between the experimental and computed vibrational spectra, we were able to unveil the most prominent bridging hydroxy μOH$^-$ displacements in the active site of HoxC (Fig. S19†). The largest μOH$^-$ displacements were correlated with the μO(H)-PVDOS profile (Fig. S19b†). In the corresponding Ni$_r$–S$_{\mu OH}^{SH}$/Ni$_r$–B$_{\mu OH}^{SH}$ models, we deduced Ni–μOH stretches at 506/494 cm^{-1} (Fig. S19c†), Fe–μOH stretches at 424/409 cm^{-1} (Fig. S19d†), and Ni–μOH–Fe wagging modes at 284/268 cm^{-1}, in which the μOH$^-$ ligand moves perpendicularly to the Ni–Fe axis of the active site. The most relevant Fe/Ni–μOH modes are depicted in Fig. 7. In spite of their inherently low ^{57}Fe-PVDOS intensities, the Ni–μOH and Fe–μOH stretches gain intensity *via* vibrational coupling to the Fe–CO/CN coordinates. They are associated with the

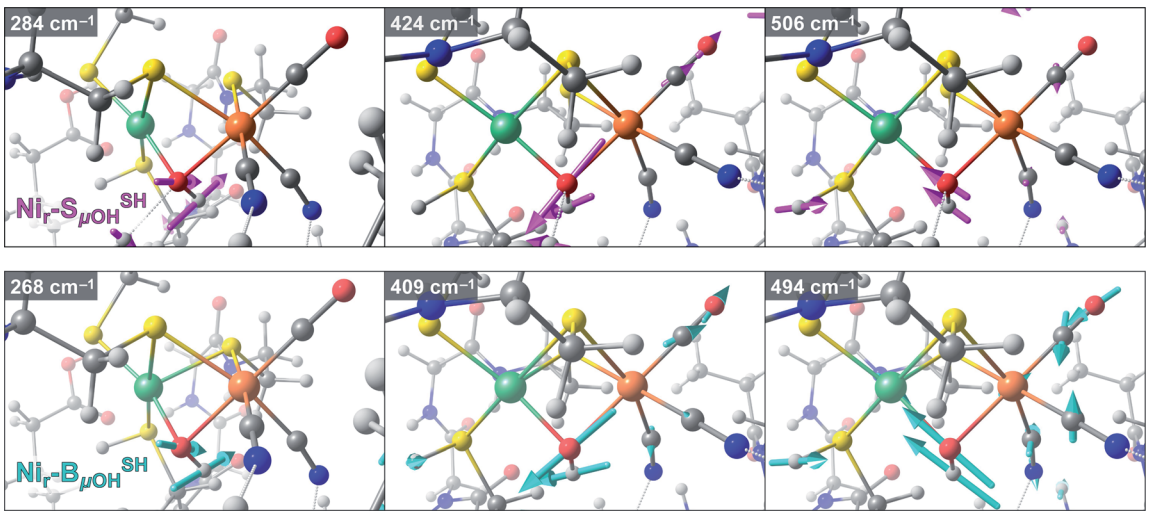

Fig. 7 Arrow-style representation of important Fe/Ni–μOH vibrational modes from representative DFT models for the Ni$_r$–S$_l$ (model Ni$_r$–S$_{\mu OH}^{SH}$, top) and Ni$_r$–B″ (model Ni$_r$–B$_{\mu OH}^{SH}$, bottom) states. The corresponding vibrational energies (cm^{-1}) are indicated in the top left of each panel. Left to right: Ni–μOH–Fe wagging, Fe–μOH stretching, and Ni–μOH stretching modes. The stick-style mode intensities relevant to the interpretation of the ^{57}Fe-PVDOS spectra are marked in Fig. S18b and S19b–d.† Animations of these and other normal modes are available as part of the ESI.†

experimental NRVS features at 507/502 (Ni–μOH) and 427/420 cm^{-1} (Fe–μOH) of Ni_r–S_I/Ni_r–B″, respectively (Fig. S16a/S17a†). Because of their relatively low intensities, no specific bands in the experimental NRV spectra could be confidently associated with the essentially pure Ni–μOH–Fe wagging modes.

Conclusions

With the present study, we provide insight into the active site structure of two interconvertible redox states of a [NiFe]-hydrogenase active site by means of vibrational spectroscopy and concomitant DFT calculations. Specific ^{57}Fe enrichment of the catalytic subunit HoxC of the regulatory [NiFe]-hydrogenase from *R. eutropha* resulted in a strong enhancement of the active site spectral features, as revealed by NRVS analysis. The absence of FeS clusters enabled the observation of low-intensity Fe–CO/CN modes as well as active site bands usually superimposed by the strong spectral contribution of FeS cluster signals. By combining NRVS with cryo-IR spectroscopy, we targeted the two hydroxy-bridged Ni_r–S_I and Ni_r–B″ states of the [NiFe] active site, which turned out to differ just in the oxidation state of the Ni ion. In fact, the two DFT-based homology models of the catalytic center Ni_r–$S^{SH}_{\mu OH}$ and Ni_r–$B^{SH}_{\mu OH}$, comprising a bridging OH^- ligand and a protonated terminal cysteine, reproduced accurately the active site bands obtained by NRV and cryo-IR spectroscopy.

Previous studies suggested a protonatable bridging hydroxy ligand between Ni and Fe ions in the Ni_r–S state(s),[21,22,39,40] whose removal produces a catalytically competent Ni_a–S intermediate.[30,41] Our results provide structural details for these states, including a protonated terminal cysteine, which is consistent with previous studies supporting a conserved protonation state in the Ni_r–B and Ni_r–S_I resting states.[22,36,37,42] Additionally, the presence of an acid-base couple (OH^- and H^+) at a close distance in the HoxC active site suggests that water removal might be a crucial step of hydrogenase maturation. This step might be mediated by the attachment of the FeS-carrying small subunit, enabling the formation of H_2-metabolizing catalytic intermediates. Recent results on the *in vitro* assembly of large and small subunits of RH from *R. eutropha* seem to corroborate this mechanism.[43]

Another important outcome of the present work is that temperature has a strong impact on the equilibrium distribution of the enzymes' redox states. Therefore, samples measured at ambient temperature by, *e.g.*, IR spectroscopy, should be used with care as a reference for experiments performed at cryogenic temperatures. This conclusion proved to be valid also for [FeFe]-hydrogenases.[44,45] It can probably be extended to the structural characterization of other biological and synthetic catalysts, where spectroscopic measurements at room temperature, *e.g.* IR, UV-visible, are used to interpret data collected using cryogenic techniques, including EPR and synchrotron-related X-ray crystallography, NRVS and XAS.

In summary, our study demonstrated the power of advanced vibrational spectroscopic techniques at cryogenic temperatures in combination with DFT calculations to elucidate the molecular active site structure of metalloenzymes. Here, we enriched and studied two hydroxy-containing redox states of [NiFe]-hydrogenases. In case catalytic intermediates can be trapped in a similar manner, this strategy will be useful to unravel their corresponding active site architectures.

Conflicts of interest

There are no conflicts to declare.

Acknowledgements

G. C., O. L., I. Z., P. H. and S. P. C. are grateful to the Einstein Foundation Berlin for funding (EVF-2016-277 and Einstein Center of Catalysis). This work was also funded by the Deutsche Forschungsgemeinschaft (DFG, German Research Foundation) under Germany's Excellence Strategy – EXC 2008 – 390540038 – UniSysCat. The authors are indebted for EU financial support (Article 38.1.2, GA) within the European Union's Horizon 2020 research and innovation program under grant agreement No 810856. S. P. C. acknowledges funding for his work through NIH GM-65440. NRVS data collection was supported by the [2017B1321], [2016B1316] and [2017A1115] SPring-8 proposals.

References

1 W. Lubitz, H. Ogata, O. Rüdiger and E. Reijerse, *Chem. Rev.*, 2014, **114**, 4081–4148.
2 H. S. Shafaat, O. Rüdiger, H. Ogata and W. Lubitz, *Biochim. Biophys. Acta Bioenerg.*, 2013, **1827**, 986–1002.
3 D. Tombolelli and M. A. Mroginski, *J. Phys. Chem. B*, 2019, **123**, 3409–3420.
4 P. A. Ash, R. Hidalgo and K. A. Vincent, *ACS Catal.*, 2017, **7**, 2471–2485.
5 R. M. Evans, E. J. Brooke, S. A. M. Wehlin, E. Nomerotskaia, F. Sargent, S. B. Carr, S. E. V. Phillips and F. A. Armstrong, *Nat. Chem. Biol.*, 2016, **12**, 46–50.
6 W. Lubitz, E. Reijerse and M. van Gastel, *Chem. Rev.*, 2007, **107**, 4331–4365.
7 M.-E. Pandelia, H. Ogata and W. Lubitz, *ChemPhysChem*, 2010, **11**, 1127–1140.
8 R. P. Happe, W. Roseboom, A. J. Pierik, S. P. J. Albracht and K. A. Bagley, *Nature*, 1997, **385**, 126.
9 J. E. Huyett, M. Carepo, A. Pamplona, R. Franco, I. Moura, J. J. G. Moura and B. M. Hoffman, *J. Am. Chem. Soc.*, 1997, **119**, 9291–9292.
10 M. Horch, J. Schoknecht, M. A. Mroginski, O. Lenz, P. Hildebrandt and I. Zebger, *J. Am. Chem. Soc.*, 2014, **136**, 9870–9873.
11 E. Siebert, M. Horch, Y. Rippers, J. Fritsch, S. Frielingsdorf, O. Lenz, F. Velazquez Escobar, F. Siebert, L. Paasche, U. Kuhlmann, F. Lendzian, M.-A. Mroginski, I. Zebger and P. Hildebrandt, *Angew. Chem., Int. Ed.*, 2013, **52**, 5162–5165.
12 S. Kamali, H. Wang, D. Mitra, H. Ogata, W. Lubitz, B. C. Manor, T. B. Rauchfuss, D. Byrne, V. Bonnefoy, F. E. Jenney, M. W. W. Adams, Y. Yoda, E. Alp, J. Zhao and S. P. Cramer, *Angew. Chem., Int. Ed.*, 2013, **52**, 724–728.

13 H. Ogata, T. Krämer, H. Wang, D. Schilter, V. Pelmenschikov, M. van Gastel, F. Neese, T. B. Rauchfuss, L. B. Gee, A. D. Scott, Y. Yoda, Y. Tanaka, W. Lubitz and S. P. Cramer, *Nat. Commun.*, 2015, **6**(1), 7890.
14 L. Lauterbach, H. Wang, M. Horch, L. B. Gee, Y. Yoda, Y. Tanaka, I. Zebger, O. Lenz and S. P. Cramer, *Chem. Sci.*, 2015, **6**, 1055–1060.
15 R. Gilbert-Wilson, J. F. Siebel, A. Adamska-Venkatesh, C. C. Pham, E. Reijerse, H. Wang, S. P. Cramer, W. Lubitz and T. B. Rauchfuss, *J. Am. Chem. Soc.*, 2015, **137**, 8998–9005.
16 E. J. Reijerse, C. C. Pham, V. Pelmenschikov, R. Gilbert-Wilson, A. Adamska-Venkatesh, J. F. Siebel, L. B. Gee, Y. Yoda, K. Tamasaku, W. Lubitz, T. B. Rauchfuss and S. P. Cramer, *J. Am. Chem. Soc.*, 2017, **139**, 4306–4309.
17 Y. Guo, H. Wang, Y. Xiao, S. Vogt, R. K. Thauer, S. Shima, P. I. Volkers, T. B. Rauchfuss, V. Pelmenschikov, D. A. Case, E. E. Alp, W. Sturhahn, Y. Yoda and S. P. Cramer, *Inorg. Chem.*, 2008, **47**, 3969–3977.
18 J. Preissler, S. Wahlefeld, C. Lorent, C. Teutloff, M. Horch, L. Lauterbach, S. P. Cramer, I. Zebger and O. Lenz, *Biochim. Biophys. Acta Bioenerg.*, 2018, **1859**, 8–18.
19 G. Caserta, C. Lorent, A. Ciaccafava, M. Keck, R. Breglia, C. Greco, C. Limberg, P. Hildebrandt, S. P. Cramer, I. Zebger and O. Lenz, *Chem. Sci.*, 2020, **11**, 5453–5465.
20 H. Tai, Y. Higuchi and S. Hirota, *Dalton Trans.*, 2018, **47**, 4408–4423.
21 S. Kurkin, S. J. George, R. N. F. Thorneley and S. P. J. Albracht, *Biochemistry*, 2004, **43**, 6820–6831.
22 B. Bleijlevens, F. A. van Broekhuizen, A. L. De Lacey, W. Roseboom, V. M. Fernandez and S. P. J. Albracht, *J. Biol. Inorg Chem.*, 2004, **9**, 743–752.
23 F. Roncaroli, E. Bill, B. Friedrich, O. Lenz, W. Lubitz and M.-E. Pandelia, *Chem. Sci.*, 2015, **6**, 4495–4507.
24 S. Frielingsdorf, J. Fritsch, A. Schmidt, M. Hammer, J. Löwenstein, E. Siebert, V. Pelmenschikov, T. Jaenicke, J. Kalms, Y. Rippers, F. Lendzian, I. Zebger, C. Teutloff, M. Kaupp, R. Bittl, P. Hildebrandt, B. Friedrich, O. Lenz and P. Scheerer, *Nat. Chem. Biol.*, 2014, **10**, 378–385.
25 M. van Gastel, M. Stein, M. Brecht, O. Schröder, F. Lendzian, R. Bittl, H. Ogata, Y. Higuchi and W. Lubitz, *J. Biol. Inorg Chem.*, 2006, **11**, 41–51.
26 Ch. Geßner, O. Trofanchuk, K. Kawagoe, Y. Higuchi, N. Yasuoka and W. Lubitz, *Chem. Phys. Lett.*, 1996, **256**, 518–524.
27 J. Fritsch, P. Scheerer, S. Frielingsdorf, S. Kroschinsky, B. Friedrich, O. Lenz and C. M. T. Spahn, *Nature*, 2011, **479**, 249–252.
28 T. Krämer, M. Kampa, W. Lubitz, M. van Gastel and F. Neese, *ChemBioChem*, 2013, **14**, 1898–1905.
29 P. E. M. Siegbahn, J. W. Tye and M. B. Hall, *Chem. Rev.*, 2007, **107**, 4414–4435.
30 H. Tai, K. Nishikawa, Y. Higuchi, Z. Mao and S. Hirota, *Angew. Chem., Int. Ed.*, 2019, **58**, 13285–13290.
31 H. Ogata, K. Nishikawa and W. Lubitz, *Nature*, 2015, **520**, 571–574.
32 A. M. Escorcia and M. Stein, *Front. Chem.*, 2018, **6**, 164.
33 G. Dong and U. Ryde, *J. Biol. Inorg Chem.*, 2016, **21**, 383–394.
34 P. E. M. Siegbahn and R.-Z. Liao, *ACS Catal.*, 2020, **10**, 5603–5613.
35 R. Breglia, C. Greco, P. Fantucci, L. De Gioia and M. Bruschi, *Inorg. Chem.*, 2019, **58**, 279–293.
36 A. L. De Lacey, A. Pardo, V. M. Fernández, S. Dementin, G. Adryanczyk-Perrier, E. C. Hatchikian and M. Rousset, *J. Biol. Inorg Chem.*, 2004, **9**, 636–642.
37 C. Fichtner, C. Laurich, E. Bothe and W. Lubitz, *Biochemistry*, 2006, **45**, 9706–9716.
38 L. Lauterbach, L. B. Gee, V. Pelmenschikov, F. E. Jenney, S. Kamali, Y. Yoda, M. W. W. Adams and S. P. Cramer, *Dalton Trans.*, 2016, **45**, 7215–7219.
39 H. Tai, L. Xu, S. Inoue, K. Nishikawa, Y. Higuchi and S. Hirota, *Phys. Chem. Chem. Phys.*, 2016, **18**, 22025–22030.
40 H. Tai, L. Xu, K. Nishikawa, Y. Higuchi and S. Hirota, *Chem. Commun.*, 2017, **53**, 10444–10447.
41 Y. Ilina, C. Lorent, S. Katz, J. Jeoung, S. Shima, M. Horch, I. Zebger and H. Dobbek, *Angew. Chem., Int. Ed.*, 2019, **58**, 18710–18714.
42 C. Stadler, A. L. de Lacey, Y. Montet, A. Volbeda, J. C. Fontecilla-Camps, J. C. Conesa and V. M. Fernández, *Inorg. Chem.*, 2002, **41**, 4424–4434.
43 G. Caserta, C. Lorent, V. Pelmenschikov, J. Schoknecht, Y. Yoda, P. Hildebrandt, S. P. Cramer, I. Zebger and O. Lenz, *ACS Catal.*, 2020, **10**, 13890–13894.
44 J. A. Birrell, V. Pelmenschikov, N. Mishra, H. Wang, Y. Yoda, K. Tamasaku, T. B. Rauchfuss, S. P. Cramer, W. Lubitz and S. DeBeer, *J. Am. Chem. Soc.*, 2020, **142**, 222–232.
45 C. Lorent, S. Katz, J. Duan, C. J. Kulka, G. Caserta, C. Teutloff, S. Yadav, U.-P. Apfel, M. Winkler, T. Happe, M. Horch and I. Zebger, *J. Am. Chem. Soc.*, 2020, **142**, 5493–5497.